

Understanding the Correlation Between Structure and Entangled Photon Pair Properties with Metal–Organic Frameworks

Published as part of *The Journal of Physical Chemistry* virtual special issue “Early-Career and Emerging Researchers in Physical Chemistry Volume 2”.

Sanoj Raj, Rubén A. Fritz, Felipe Herrera, and Yamil J. Colón*



Cite This: <https://doi.org/10.1021/acs.jpcc.3c00355>



Read Online

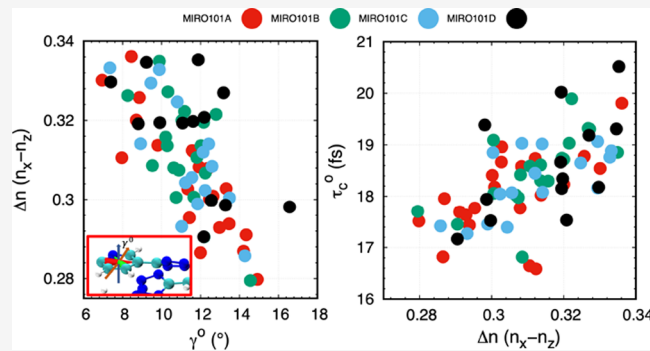
ACCESS |

Metrics & More

Article Recommendations

Supporting Information

ABSTRACT: Spontaneous parametric down conversion (SPDC) is a quantum second-order nonlinear optical process where the photons generated are frequently used in quantum information processing. Materials with large second-order nonlinearities ($\chi^{(2)}$) can be used as entangled photon sources with a high brightness. The source brightness scales as the square of the effective nonlinearity (d_{eff}), which is an intrinsic property of the material. Understanding material factors that can significantly alter this intrinsic property is useful in developing new materials that are SPDC efficient. In our work we focus on understanding factors affecting the entangled photon pair properties, such as the arrangements of ligands within the $\text{Zn}(3\text{-ptz})_2$ metal–organic framework (MOF) crystal and temperature. We find that the arrangement and alignment of the pyridine rings in the crystal structure significantly affect the d_{eff} and birefringence (Δn). Smaller pyridine ring alignments relative to the optic *c*-axis increase the Δn , which in turn leads to larger photon pair correlation times (τ_c) in coincidence measurements. Our work has significant implications in understanding the effect of ligand arrangement on d_{eff} and τ_c for any MOF crystal structure, providing a tool to rationalize the optimization of MOF crystals for the development of efficient nonlinear optical devices.



INTRODUCTION

Spontaneous parametric down-conversion (SPDC) is a second-order nonlinear optical process in which a photon of high frequency incident on a nonlinear material is converted into two photons of lower frequencies. The incident photon is referred to as the pump and the converted photons coming out from the material are called signal and idler.¹ SPDC is parametric because the pump photon splitting into pairs of photons happens in accordance with conservation laws: sum of the momenta of the signal and idler photons is equal to the momentum of the pump photon, and the sum of the energies is equal to energy of the pump photon.¹ This process is at the center of many quantum optics applications such as quantum information,^{2,3} quantum computing,^{4,5} quantum cryptography,^{6–8} imaging,^{9–11} quantum dense coding, and quantum metrology,^{12,13} and is also used in studying the foundations of quantum mechanics. Materials with a large second-order nonlinear optical (NLO) susceptibility ($\chi^{(2)}$) play a crucial role in developing modern optical and electro-optical devices as well as entangled photon sources with high brightness.

For crystals that support a perfect phase matching condition (PPM),¹⁴ the second harmonic generation (SHG) intensity

scales linearly with propagation length (L)^{15,16} when crystals have a random orientation (powder) and scales as L^2 for a single crystal. This quadratic scaling offers a benefit for SPDC because it maximizes the brightness of the nonclassical signal (number of entangled photon pairs) and optimizes the degree of temporal correlations in coincidence detection (photon indistinguishability), which leads to the entanglement of photonic degrees of freedom.¹⁷ The brightness of the signal scales as the square of the effective nonlinearity (d_{eff}^2), which is an intrinsic property of the material and can be easily computed from first principles. The d_{eff} is used to parameterize an effective Hamiltonian for the SPDC process. It is obtained by contracting the $\chi^{(2)}$ tensor with the appropriate input and output field polarizations. The number of entangled photon pairs produced by the material as well as the temporal and

Received: January 16, 2023

Revised: May 10, 2023

Published: May 30, 2023

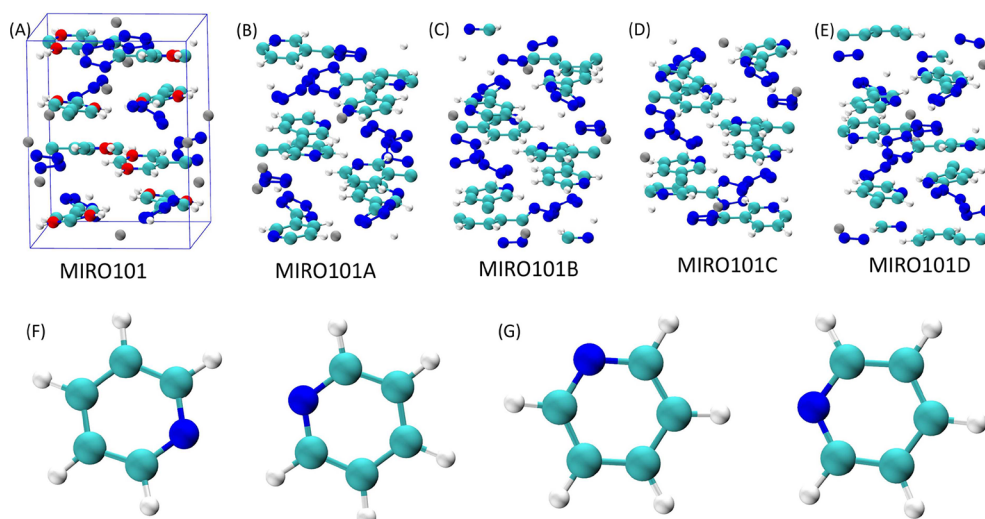


Figure 1. (A) (MIRO101, CSD: 184958) Cyan, white, blue, and gray represent carbon, hydrogen, nitrogen and zinc atoms. Red ball can be either nitrogen or carbon. (B–E) Prepared structures of MIRO101 obtained by choosing a red ball in (A) to be either carbon or nitrogen. (F) and (G) show two arrangements of pyridine rings which are present in the MIRO101A–D crystal structures.

spectral properties of the entangled pair wave function can be computed from an effective nonlinear Hamiltonian in first order perturbation theory.^{18,19}

SHG ($\omega \rightarrow 2\omega$) and SPDC ($2\omega \rightarrow \omega$) are conjugate processes in nonlinear optics that differ on how they are experimentally implemented. The frequency conversion efficiency of SHG and SPDC in a given crystal is determined by the same components of the nonlinear susceptibility tensor ($\chi_{ijk}^{(2)}$). Understanding the SHG efficiency with respect to the material factors will be useful for SPDC experiments. The efficiency of SHG is significantly affected by the degree of noncentrosymmetry (point groups can be polar, chiral, both, or neither), size of the crystal, donor–acceptor bonds, π -electron delocalization, anisotropy, and temperature.^{20,21} Various inorganic materials, such as KDP, BBO,^{22,23} LiNbO₃,²⁴ quartz, and others, have been experimentally realized for the nonlinear optical process, but have revealed deficiencies such as an absence of electron delocalization and the inability to adjust structures. Organic materials have been proposed to resolve these deficiencies, but they lack good mechanical strength and thermal stability. Metal–organic frameworks (MOFs) are hybrid materials that have shown promise for the nonlinear optical process,^{25–27} as they can combine the benefits of inorganic and organic classes of compounds. MOFs offer interesting possibilities in terms of the synthesis of new structures with high precision and predictability in the desired properties of the final products. Several MOF structures have been experimentally synthesized, and some of them have already shown potential to be used in a nonlinear optical response.^{21,28–30} Understanding the structure and nonlinear property relationship of these MOFs can lead to the discovery of novel materials that are SHG/SPDC efficient.^{31–33} Ab initio calculations can provide a valuable tool to predict the optical properties of the MOF crystals and predict the important material factors that are responsible for a higher second-order nonlinear optical response.¹⁹

Our work focuses on understanding how factors such as different arrangements of ligands within the crystal and thermal molecular motions affect d_{eff} group velocity dispersion (GVD), entangled photon pair correlation times (τ_c), and the phase matching angle (θ_m) in MOFs. Our paper is divided into 3

sections. Section 1 describes the method used in our study, section 2 describes the effect of ligand arrangements within the unit cell on d_{eff} and τ_c , and section 3 describes how thermal motion affects these observables.

METHODS

We focus on catena-(bis(μ_2 -5-(3-pyridyl)tetrazolato)-zinc(II)) ($\text{Zn}(3\text{-ptz})_2$) MOF (MIRO101, Wang et al. *Inorganic Chemistry*, 2003, 42, 3969) in our study to understand how ligand arrangements in the crystal structure and thermal molecular motions at 300 K affect the entangled photon pair properties. We have used VESTA³⁴ to manipulate the original cif file, which was obtained from CCDC, and prepare different crystal structures. There are 8 pyridine ligands present in the original cif file (Figure 1A) that can give different combinations of ligand arrangements in the crystal structure. Atoms shown with red balls in Figure 1A can be either carbon or nitrogen. Figure 1B–E shows the four possible MIRO101 structures prepared by choosing red balls to be either carbon or nitrogen. We refer to these as MIRO101A, MIRO101B, MIRO101C, and MIRO101D. These structures differ in the arrangement of the pyridine ligands. Figure 1F,G shows the two different arrangements of the pyridine ligands that can be found in the prepared crystal structures. We were able to prepare these structures because the two atoms in the pyridine rings have an occupancy of 0.5 in the cif file. The arrangements of the ligands discussed in our study will be present in the real crystal, considering there is no clarity of which is the ultimate relative position inside the unit cell, as the MOF self-assembly process is limited. For example, freely rotating the pyridine group can give MIRO101A and MIRO101B. The experimentally measured properties (effective nonlinearity and photon pair correlation time) will compare better with the average values obtained for different crystals studied here.

The software suite ISOTROPY³⁵ was used to identify the space group of the prepared structures. All the crystal structures were optimized using the POB-DZVPP basis set with shrink points 3 3 and TOLINTEG 12 12 12 12 18. We also added DFT-D version 4 for the dispersion correction. We used solid-state DFT within the Coupled Perturbed Hartree–

Fock/Kohn–Sham method (CPHF/KS)^{36–38} with a PBE functional to compute the dynamical dielectric tensor $\epsilon_{ij}(\omega)$ and the dynamical second-order susceptibility tensor $\chi_{ijk}^{(2)}(\omega)$ of the optimized structures. We used the CRYSTAL17³⁹ package to carry out all the DFT calculations. The dynamical dielectric tensor was used to obtain the Sellmeier equations for ordinary (o) and extraordinary (e) crystal axes over a frequency range from the near-infrared up to the crystal band gap. We fit the ab initio curves to the standard relation

$$n_{i=o,e}^2(\lambda) = A + \frac{B\lambda^2}{\lambda^2 - C} + \frac{B_1\lambda^2}{\lambda^2 - C_1} \quad (1)$$

to obtain the Sellmeier coefficients for each crystal structures and crystal axis (n_o and n_e). The Sellmeier coefficients were used to establish PPM¹⁴ for the e-oo degenerate collinear type-I SPDC¹⁸ (pump and signal photons share the same propagation direction k) with signal output at 1064 nm. The obtained $\chi^{(2)}$ from the CPHF/KS calculation is used to evaluate the d_{eff} . The d_{eff} is obtained by contracting the $\chi^{(2)}$ tensor with the appropriate input and output field polarizations. All the crystal structures considered in our study are negative uniaxial ($n_o > n_e$). We calculate the phase matching angle from the Sellmeier curve using the equation:

$$\sin^2(\theta_m) = \frac{n_e^2(2\omega)}{n_o^2(\omega)} \frac{(n_o^2(2\omega) - n_o^2(\omega))}{(n_o^2(2\omega) - n_e^2(2\omega))} \quad (2)$$

θ_m is the angle between the propagating vector and the optic axis and is used to achieve optimal three-wave mixing for collinear e-oo type-I phase matching. Figure 2 shows the configuration used for the estimation of d_{eff} .

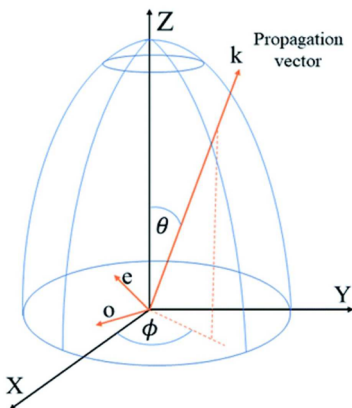


Figure 2. Polarization configuration used for the estimation of the effective nonlinearity (d_{eff}) in e-oo type-I phase matching. Adapted from Fritz, R. A.; Colón, Y. J.; Herrera, F. Engineering entangled photon pairs with metal–organic frameworks. *Chem. Sci.* 2021, 3478, under CC BY-NC 3.0 (Attribution-NonCommercial 3.0 Unported).

For a pump field at frequency ω , wavevector k , and the polarization vector \hat{e}_e along the ordinary axis, an entangled photon pair is produced via SPDC with an ordinary polarization \hat{e}_o . In the collinear case, all waves propagate at an angle θ relative to the optic axis of the crystal (Z direction). d_{eff} was estimated using a specific configuration by contracting the full second-order polarizability tensor at phase matching angle for different crystal structures at 1064 nm. The electric field component in the ordinary axis is given by $E_j^o(\omega) = (a_j)$

$E^o(\omega)$ and the electric field component in the extraordinary axis is given by $E_j^e(\omega) = (b_j)E^e(\omega)$, where

$$(a_j) = \begin{pmatrix} \sin \phi \\ -\cos \phi \\ 0 \end{pmatrix}, \quad (b_j) = \begin{pmatrix} -\cos \theta \cos \phi \\ -\cos \theta \sin \phi \\ \sin \theta \end{pmatrix} \quad (3)$$

For type-I negative uniaxial, d_{eff} is calculated as

$$P(\omega_3) = b_i d_{ijk}(\omega_3, \omega_2, \omega_1) a_j a_k E_j(\omega_2) E_k(\omega_1) \quad (4)$$

$P(\omega_3)$ is the dielectric polarization of the crystal at the pump frequency $\omega_3 = \omega_1 + \omega_2$ ($\omega_3 = 2\omega$ and $\omega_2 = \omega_1 = \omega$). A conventional eoo type-I condition was used,¹⁴ where the entangled signal and idler are polarized along the ordinary axis (o) and the pump is polarized along the extraordinary axis (e).

The calculations of photon pair properties closely follow our previous work.¹⁹ We obtain the d_{eff} at the perfect phase matching θ_m at 1064 nm, group velocity dispersion (GVD or β_2) from the Sellmeier curve, and the correlation time τ_c for ordinary and extraordinary signal field polarizations. We have also estimated the photon pair correlation time τ_c for a given coincidence detection bandwidth σ . The material GVD is calculated as⁴⁰

$$\text{GVD}_{i=o,e} = \frac{\lambda^3}{2\pi c^2} \frac{d^2 n_i}{d\lambda^2} \quad (5)$$

where $d^2 n_i / d\lambda^2$ is the second derivative of the refractive index with respect to wavelength at $\lambda_s = 1064$ nm for degenerate signal and idler fields (eq 1), and c is the speed of the light. The correlation time τ_c for SPDC under collinear type-I phase matching is approximately $2.0\tau_L$ in the broadband detection limit ($\sigma \gg 1/\tau_L$). The characteristic crystal time scale, $\tau_L = \sqrt{L\beta_2/4}$, is roughly the width of the two-photon intensity correlation function $G^{(2)}$.

To study the effect of temperature on d_{eff} and entangled photon pair properties, we computed the $\chi^{(2)}$ of the frames extracted from the molecular dynamics (MD) simulation of different MIRO101 optimized crystal structures with a signal output at 1064 nm. Large-scale Atomic/Molecular Massively Parallel Simulator (LAMMPS)⁴¹ in a NVT ensemble was used to perform MD simulations with a time step of 1 fs at 300 K, and simulations were run for 1 ns. The Lammmps interface⁴² was used to prepare the LAMMPS data file with UFF force field parameters. The Lammmps interface created a $3 \times 3 \times 2$ supercell as the unit cell that was not large enough to support a nonbonded cutoff of 12.5 Å. We extracted the atoms that were part of the original unit cell and reconstructed the unit cell with ab initio optimized cell parameters.

To study the wave function of the entangled photon pairs generated by noncentrosymmetric MOFs via SPDC, we compute the $G^{(2)}$ intensity correlation function for coincidence detection of the entangled pairs produced under the collinear type-I phase matching condition described above. The width of the $G^{(2)}$ function gives the pair correlation time τ_c , which is a measure of the indistinguishability of the two photons in a pair. The probability of detecting a photon at time t_1 , and a second photon at time t_2 is proportional to the (unnormalized) intensity correlation function $G^{(2)}(t_1, t_2) = |\langle 0 | \hat{E}^{(+)}(t_2) \hat{E}^{(+)}(t_1) | \Psi_2 \rangle|^2$, where $\hat{E}^{(+)}(t_j)$ is a far-field operator that takes into account any spectral filtering done at the detectors and $|\Psi_2\rangle$ is the biphoton wave function

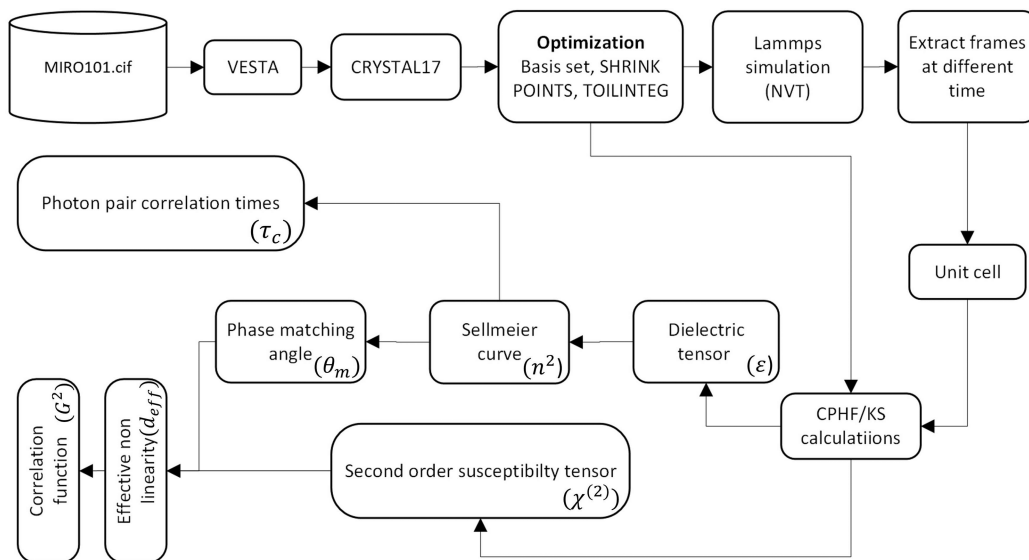


Figure 3. Flowchart for the calculation of entangled photon pair properties.

Table 1. Space Group, Optimized Cell Parameters, Total Energy, and Band Gap of MIRO101A–D Crystal Structures

MOF	space group	cell parameters	energy (AU)	band gap (eV)
MIRO101A	84	$a = b = 10.1580 \text{ \AA}$, $c = 13.2933 \text{ \AA}$, $\alpha = \beta = \gamma = 90.0$	-11147.8488	3.14
MIRO101B	4	$a = 10.1309 \text{ \AA}$, $b = 10.1314 \text{ \AA}$, $c = 13.3416 \text{ \AA}$, $\alpha = \gamma = 90.0$, $\beta = 90.2$	-11147.9002	3.08
MIRO101C	1	$a = 10.1529 \text{ \AA}$, $b = 10.1448 \text{ \AA}$, $c = 13.250 \text{ \AA}$, $\alpha = 90.1560$, $\beta = 90.3$, $\gamma = 90.9192$	-11147.8899	3.06
MIRO101D	4	$a = 10.0378 \text{ \AA}$, $b = 10.2637 \text{ \AA}$, $c = 13.2849 \text{ \AA}$, $\alpha = \gamma = 90.0$, $\beta = 90.5$	-11147.7722	3.05

that describes the coherent conversion of pump photons from a strong visible laser field into photon pairs. The actual number of entangled photon pairs produced by a crystal (brightness) can be calculated for perfect crystals by knowing the pump spectral profile, the transverse intensity profiles of the pump and signal fields, and the propagation length. The source brightness scales with d_{eff}^2 which is an intrinsic property of the crystals that can be evaluated from first principles.¹⁹ Figure 3 shows the systematic flowchart of our methodology for calculating entangled photon pair properties.

Gaussian 16⁴³ was used to calculate the dipole electric field hyperpolarizabilities for different arrangements (shown in Figure 1F,G) of the pyridine ligands using the 6-311g(d,p) basis set with a B3LYP functional. The pyridine rings arrangement was obtained from the optimized crystal structures by removing tetrazole ligands that are attached to pyridine rings with hydrogen. We have calculated the hyperpolarizabilities with the desired frequency by including CPHF = RdFreq in our input file.

To find the average d_{eff} at a given temperature, we have used the Boltzmann distribution to calculate the probability of a certain state as a function of energy as

$$p_i = \frac{e^{-E_i/kT}}{\sum_{j=1}^m e^{-E_j/kT}} \quad (6)$$

where p_i is the probability of the state i , E_i is the energy of the state i , k_B is the Boltzmann constant, T is the temperature of the system, and m is the number of states accessible to the system of interest. In our calculation, we extract different frames from MD simulations for a given system. We calculate the SCF energy (energy/atom) of the extracted frames and

find the probability using eq 6 for a given state. We calculate the average d_{eff} using

$$\langle (d_{\text{eff}})^2 \rangle = \sum_{i=1}^m p_i \times (d_{\text{eff}}^i)^2 \quad (7)$$

where p_i is the extracted frame i probability, d_{eff}^i is the d_{eff} of the frame i , and m is the total number of frames extracted from the MD simulations.

RESULTS AND DISCUSSION

The optical classification of the various crystal systems is based on which symmetry class a given crystal belongs to. Triclinic, monoclinic, and orthorhombic crystal systems are classified as biaxial; trigonal, tetragonal, and hexagonal crystal systems are classified as uniaxial; and cubic crystal systems are classified as isotropic.¹⁴ In terms of the refractive index of the crystals, the uniaxial crystal exhibits two distinct principal refractive indices, $n_X = n_Y \neq n_Z$, and biaxial crystals exhibit three unequal principal refractive indices, $n_X \neq n_Y \neq n_Z$, along the principal optic axis. Isotropic crystals have a single principal refractive index, $n_X = n_Y = n_Z = n$. In our study, we have used the crystal class of the structures to classify a given crystal into uniaxial, biaxial, or isotropic. All the structures described in Figure 1B–E exhibit anisotropic linear optical properties and consequently display the property of birefringence (Δn ($n_x - n_z$ or $n_y - n_z$) $\neq 0$).

Based on the space group obtained of the prepared crystal structures using ISOTROPY,³⁵ MIRO101A is uniaxial and MIRO101B–D are biaxial. Table 1 shows the band gap (E_g), space group, optimized cell parameters, and the total energy of all the MIRO101A–D crystal structures. MIRO101A belongs to the $\bar{4}2m$ crystal class and MIRO101B–D crystal structures

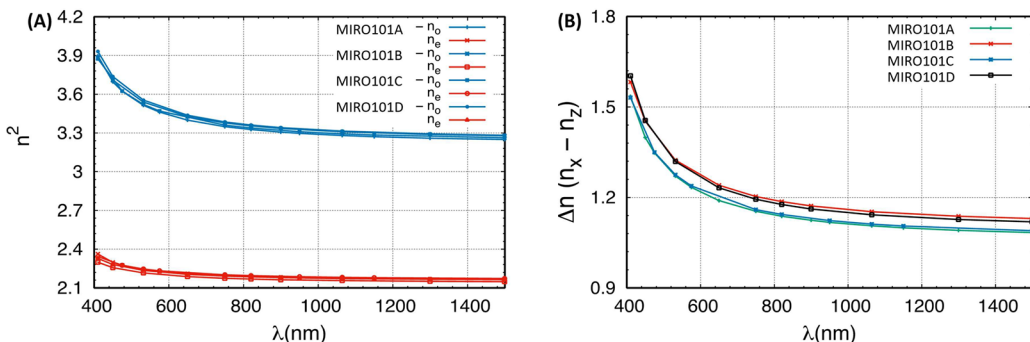


Figure 4. (A) Sellmeier curves of MIRO101A–D crystal structures. (B) Birefringence (Δn) at different signal wavelengths.

Table 2. Birefringence at 1064 nm, Phase Matching Angle θ_m , d_{eff} Evaluation at the Propagation Direction (θ_m, ϕ) in Collinear Type-I SPDC at 1064, GVD at PPM for Ordinary (o) and Extraordinary (e) Propagation Directions, and Photon Pair Correlation Times τ_c^a

MOF	birefringence ($\Delta n (n_x - n_z)$)	phase matching angle (θ_m ; deg)	d_{eff} (pm/V)	ϕ (deg)	γ° (deg)
MIRO101A	0.3364	20.80	0.36 −0.36	80 170	5.24
MIRO101B	0.3506	19.96	0.12	90	4.65 ± 0.05
MIRO101C	0.3376	20.45	0.17	90	7.09 ± 2.92
MIRO101D	0.3467	20.51	−0.17	90	7.27 ± 1.29

^aWe have set the crystal length to $L = 1.5$ mm for our correlation time calculation.

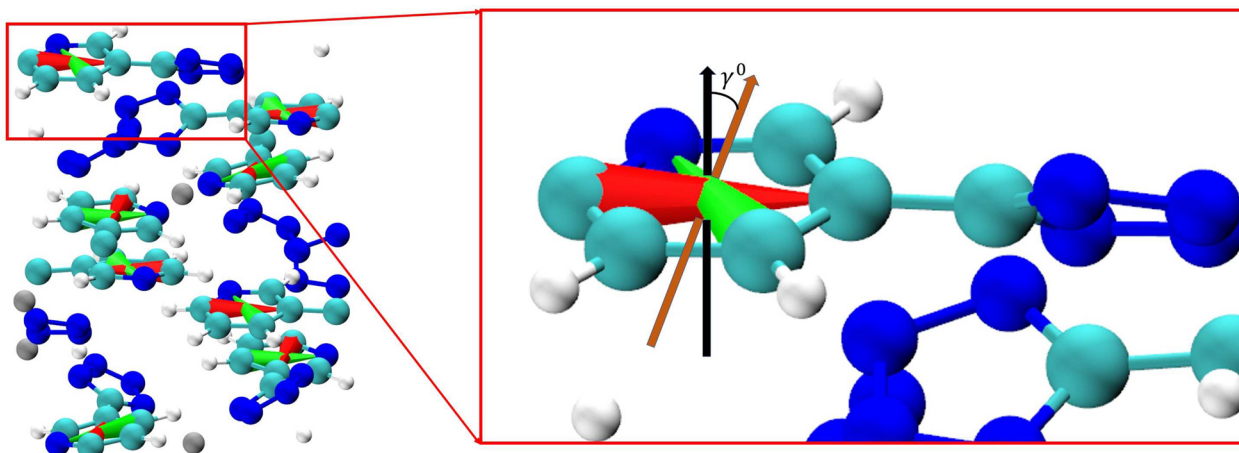


Figure 5. Pyridine ring alignment (γ°). γ° is the angle between the normal vector (obtained from red and green vectors represented by the cone for the pyridine ring) shown with a brown arrow and the z -axis (c -axis) shown with a black arrow.

belong to crystal class 2, 1, and 2, respectively. Although MIRO101B–D are biaxial, one can always fix the crystal orientation such that light propagation is influenced by two refractive indices only.⁴⁴ For a biaxial crystal, we have picked the axis that gives the highest Δn and use those refractive indices to calculate the phase matching angle (θ_m). MIRO101B has the lowest energy with a band gap of 3.08 eV and MIRO101A has the highest energy with a band gap of 3.14 eV.

Phase Matching Angle and Effective Nonlinearity. Figure 4A shows the Sellmeier curves ($n^2(\lambda)$) of all the crystal structures (MIRO101A–D) along the ordinary axis (n_o) and the extraordinary c -axis (n_e). We obtain $n^2(\lambda)$ for our crystal structures from dielectric tensor $\epsilon_{ij}(\omega)$ computed at different wavelengths (see flowchart in the Methods section). We fit the ab initio curves to eq 1 to obtain the Sellmeier coefficients for all MIRO101A–D structures. The Sellmeier coefficients of all these crystal structures are shown in Table S1. Figure 4B shows

the Δn of different MIRO101 structures as a function of wavelength. We have calculated θ_m at 1064 nm for all the MIRO101A–D crystal structures using eq 2 and refractive index values in Table S2. Table 2 shows the Δn and θ_m of all the crystal structures (Figure 1B–E).

We have adopted eoo type-I conditions to calculate the d_{eff} at the θ_m . We have evaluated d_{eff} using eq 4 for all the crystal structures used in our study. For the uniaxial crystal (MIRO101A), we optimize d_{eff} for ϕ , whereas for biaxial crystals (MIRO101B–D), we set ϕ to be 90°. Figure S1 shows the computed $\chi^{(2)}$ for all the crystal structures. γ° , shown in Table 2, is the pyridine ring alignment with respect to the Z -axis (c -axis). We have calculated the average pyridine ring alignment (γ°) in Figure 5, for the MIRO101A–D crystal structures. To calculate γ° , we considered two vectors (shown in the red and green cone in Figure 5) for all the pyridine rings in the unit cell. We take the cross product of these vectors and

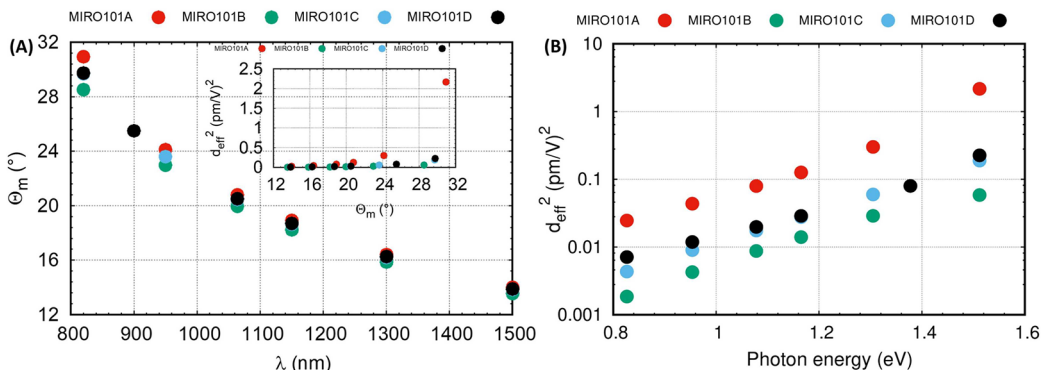


Figure 6. (A) Perfect phase matching angle θ_m for MIRO101A–D crystal structures for a range of signal wavelengths. (inset) d_{eff}^2 for MIRO101A–D crystal structure at PPM. (B) d_{eff}^2 for the MIRO101A–D crystal structure as a function of photon energy.

then find the angle between the normal vector and Z-axis vector (*c*-axis). γ° indicates the planarity of the pyridine rings in the crystal structure in the XY plane. A smaller value of γ° indicates that the pyridine rings in the crystal structure are more planar than a higher value of γ° . Table 2 shows the d_{eff} for all the crystal structures considering the d_{eff} configuration in Figure 2. We find that different crystal structures have different d_{eff} (sign is unimportant because the d_{eff}^2 profile specifies conversion efficiency) and the average of the $|d_{\text{eff}}|$ values will be closer to the experimentally observed d_{eff} value. The d_{eff} value for a real crystal should be around 0.205 pm/V.

To understand why the MIRO101A–D structures that only differ in the pyridine rings arrangement give rise to different d_{eff} , we have calculated the hyperpolarizability (β) of different arrangements of pyridine ligands that are present in the MIRO101A–D crystal structures. The two pyridine ring arrangements of interest are shown in Figure 1F,G. We call arrangement 1 the arrangement where the nitrogen atoms of the adjacent pyridine rings are facing toward each other, and arrangement 2 is where the nitrogen atoms of the adjacent pyridine rings are facing away from each other. In order to understand how these two arrangements might affect the d_{eff} , we have extracted the positions of these arrangements from the optimized unit cell and calculated the hyperpolarizability (β) using Gaussian 16 at 1064 nm. We observe that arrangement 1 has a net dipole moment of -0.40 D (pointing toward the crystal optical axis (Z axis)) and has $\beta = 17.89$ au parallel to the Z axis. Arrangement 2 has a net dipole moment of 4.86 D (pointing in the XY plane) and has a β of 5.46 au parallel to the Z axis. Based on our configuration used for estimating d_{eff} , higher values of β in the Z direction should give higher d_{eff} . From our results, we do observe that MIRO101A has a higher d_{eff} , which has all the pyridine rings with arrangement 1, than MIRO101B, which has all the pyridine rings with arrangement 2. MIRO101C and MIRO101D have less oriented pyridine ring arrangements, which might explain why the d_{eff} values are different. We clearly see from our calculations that the arrangement of the pyridine rings can significantly affect β and thus d_{eff} .

The orientation of the ligands in the crystal can significantly affect the refractive indices as well.⁴⁵ Table 2 shows the Δn and averaged γ° for all the crystal structures. We find that the ring alignment does have an effect on the Δn , which can in turn affect the θ_m . The effect of γ° on Δn and θ_m is discussed in more detail later. To understand how θ_m and d_{eff} depend on signal wavelength, we have done CPHF/KS calculation for a range of signal wavelengths. Figure 6A shows θ_m at different

signal wavelengths and Figure 6B shows the d_{eff}^2 (generated power depends on d_{eff}^2) as a function of photon energy. We observe that θ_m decreases with increasing signal wavelength, and d_{eff}^2 increases with increasing photon energy. We also observe that d_{eff}^2 value scales differently for different MIRO101A–D structures. MIRO101A crystal structure d_{eff}^2 is very different at higher photon energy compared to MIRO101B–D crystal structures as shown in Figure 6B. This can be due to the d_{eff} configuration used in our calculations. These results suggest that the arrangement of ligands in the crystal structures can give significantly different d_{eff} at different signal wavelengths. We have tried to understand the correlation between γ° , Δn , θ_m , and d_{eff}^2 in our temperature-dependent study, as discussed in a later section.

Table 3 summarizes the SPDC with collinear type-I phase matching results for MIRO101A–D crystals with $L = 1.5$ mm.

Table 3. Birefringence at 1064 nm, Phase Matching Angle θ_m , d_{eff} Evaluation at the Propagation Direction (θ_m , ϕ) in the Collinear Type-I SPDC at 1064, GVD at PPM for Ordinary (o) and Extraordinary (e) Propagation Direction, and Photon Pair Correlation Times τ_c^a

MOF	GVD _o (fs ² mm ⁻¹)	GVD _e (fs ² mm ⁻¹)	τ_c^o (fs)	τ_c^e (fs)
MIRO101A	213.43	78.12	17.89	10.82
MIRO101B	211.43	69.38	17.82	10.20
MIRO101C	209.60	74.43	17.73	10.57
MIRO101D	218.88	73.39	18.12	10.49

^aWe have set the crystal length to $L = 1.5$ mm for our correlation time calculation.

We observe that the photon pair correlation time is different for different MIRO101A–D crystal structures, which differ in the pyridine ring arrangement in the unit cell. The experimentally observed correlation time will compare better with the average photon pair correlation time of different crystals (MIRO101A–D).

Temperature Effect on Effective Nonlinearity and Entangled Photon Pair Properties. The MOF observables shown in Tables 2 and 3 can be affected by temperature because the thermal lattice distortions are known to influence optical properties.^{46–49} To understand how the MOF observables are affected by temperature, we have done MD simulations of all the crystal structures shown in Figure 1B–E at 300 K using LAMMPS (see the Methods section). We ran single point calculations to estimate the band gap of all the extracted frames. We picked several frames whose band gap

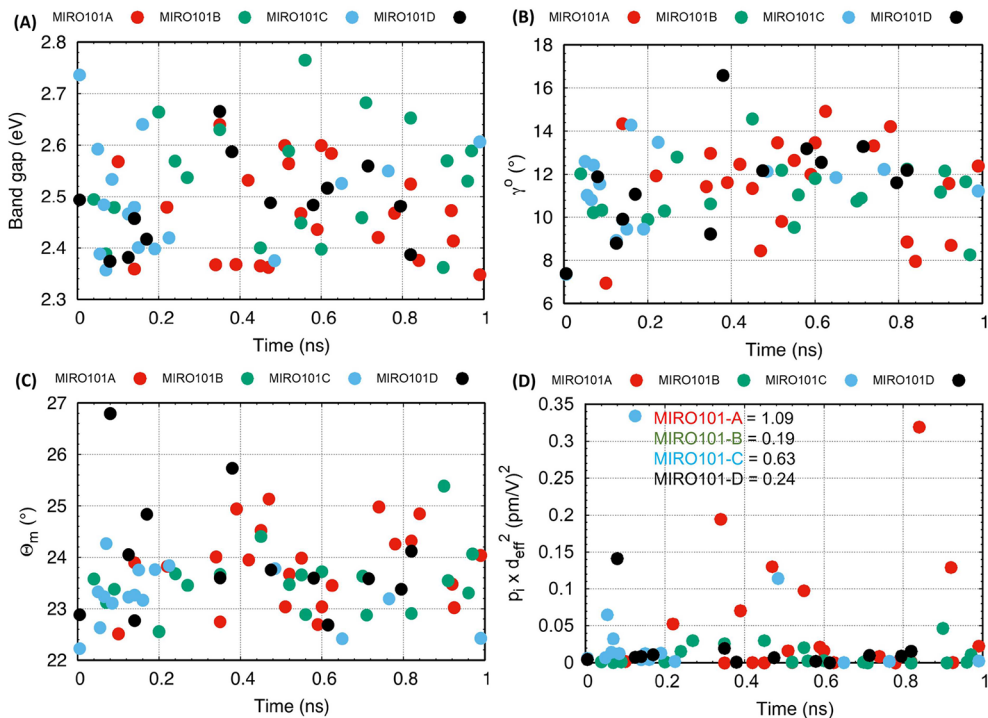


Figure 7. (A) Band gap of extracted frames from MD simulations for all the crystal structures (MIRO101A–D) at different times. (B) Pyridine ring alignment (γ°) of extracted frames from MD simulations for all the MIRO101A–D crystal structures at different time. (C) Phase matching angle (θ_m) of extracted frames from MD simulations for all the MIRO101A–D crystal structures at different times. (D) Probability associated with different frames times the d_{eff}^2 (θ_m of the optimized structure and $\phi = 90^\circ$) for all the crystal structures (MIRO101A–D) at different times. Average value of d_{eff}^2 for all the crystal structures (MIRO101A–D) at $T = 300$ K is shown in the inset. Red, green, blue, and black circles represent the MIRO101A, MIRO101B, MIRO101C, and MIRO101D, respectively.

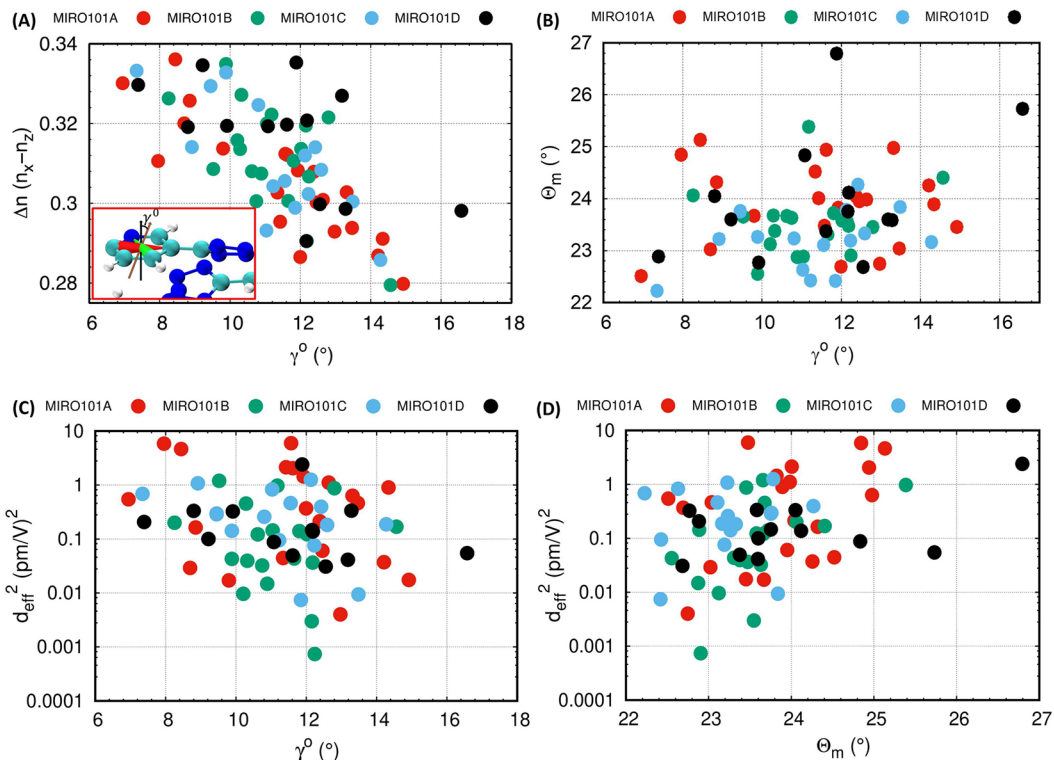


Figure 8. (A) Birefringence (Δn) as a function of pyridine ring alignment (γ°) of all the extracted frames. (B) Phase matching angle (θ_m) as a function of pyridine ring alignment (γ°) of all the extracted frames. (C) d_{eff}^2 calculated using fixed θ_m of the optimized structure and $\phi = 90^\circ$ all the extracted frames as a function of γ° . (D) d_{eff}^2 calculated using θ_m calculated at 1064 nm and $\phi = 90^\circ$ of respective frames. Red, green, blue, and black circles represent the MIRO101A, MIRO101B, MIRO101C, and MIRO101D, respectively.

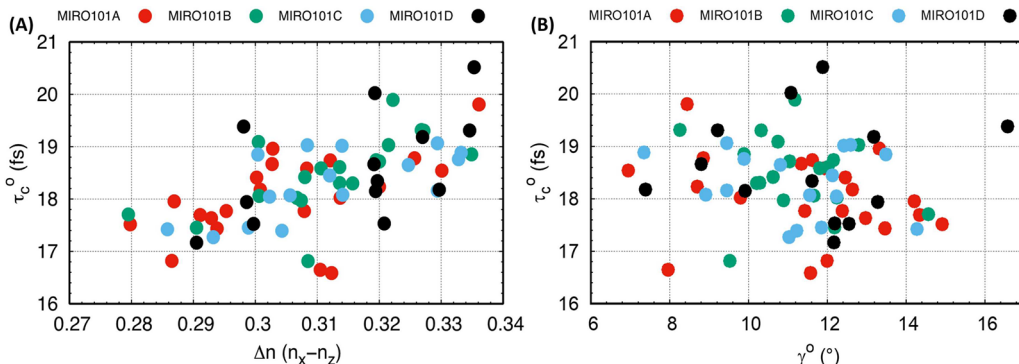


Figure 9. (A) Entangled photon pair correlation times (τ_c) as a function of birefringence (Δ_n) for different frames extracted from MD simulations. (B) Entangled photon pair correlation times (τ_c) as a function of pyridine ring alignment (γ°) for different frames extracted from MD simulations.

were greater the 2.33 eV (two times the pump photon energy). Figure 7A–C show the band gap, γ° , and θ_m of all the extracted frames of all the crystal structures used in the following calculations. We imposed the condition to have our Sellmeier curves starting from 532 nm. As expected, the band gap, γ° , and θ_m fluctuate with time. Band gap values lie between 2.34 and 2.78 eV, γ° lies between 6.79° and 16.78°, and θ_m lies between 22.2° and 26.7° for all the structures studied. The decrease in the band gap is due to the weakening of interatomic bonds due to increase in temperature.

We performed the CPHF/KS calculation on the frames extracted from MD simulations to calculate ϵ and $\chi^{(2)}$. To calculate the average d_{eff} at $T = 300$ K, we used Boltzmann averaging for all the frames (see eqs 6 and 7). Extracted frames energy and probability associated with the frames are shown in Figure S2 for all the MIRO101A–D crystal structures. To calculate the effective nonlinearity d_{eff} for each frame, we have used the phase matching angle (θ_m) of the optimized structure (see Table 1) and $\phi = 90^\circ$. Figure 7D inset shows the average d_{eff}^2 of all the crystals structures at $T = 300$ K. MIRO101 is a crystal structure where two atoms have partially occupancy of 0.5 and the ligand arrangements considered in our study by considering different crystal structures (1B–E) reflect that partial occupancy. The d_{eff}^2 will be the outcome of all different possibilities of ligands arrangements in the crystal structure. We can estimate the d_{eff}^2 of MIRO101 structure (1A) by averaging the d_{eff}^2 of all the MIRO101A–D crystal structures. We estimate $d_{\text{eff}}^2 = 0.54 \text{ pm}^2/\text{V}^2$ at $T = 300$ K for MIRO101 crystal, which has yet to be shown experimentally. Figure S3B shows the d_{eff}^2 of all the extracted frames with θ_m calculated at 1064 nm and fixing $\phi = 90^\circ$. We observe that different frames have different d_{eff} .

We observe a strong correlation between Δn and the pyridine ring alignment (γ°), as shown in Figure 8A. Δn values increase with a decrease in γ° , which is due to the π electrons contributing differently to in-plane and out-of-plane directions, leading to difference in Δn . This result suggests that the different frames have different anisotropy leading to different $\chi^{(2)}$ ⁵⁰ and, therefore, different d_{eff}^2 . We also find that γ° barely affects the θ_m (Figure 8B). We hardly see any correlation γ° and θ_m with d_{eff}^2 as shown in Figure 8C,D. We did observe that the d_{eff}^2 for MIRO101A crystal structure compared to MIRO101B–D crystal structures, as shown in Figure 8D, is very different at higher θ_m . It appears that the d_{eff}^2 for MIRO101A has similar trend with θ_m , which was observed above in our d_{eff}^2 versus signal wavelength study (see Figure 6A, inset).

Figure S4 shows the Sellmeier curves of all the extracted frames for different MIRO101A–D crystal structures. We calculated the entangled photon pair properties of the frames extracted from different crystal structures using eq 5. Figure 9 shows how τ_c° is affected by the γ° and Δn (γ° affects Δn) in the crystal structure. We observe a strong correlation between Δn and the photon pair correlation times τ_c . We observe that τ_c° decreases with increasing γ° and increases with Δn . These results suggest that the planarity of the pyridine rings can be used to control the anisotropy of the crystal structures, which can significantly affect the photon pair correlation times that are used in entanglement-based applications. Larger Δn leads to faster dephasing of the generated photons for type II, but for the type I, the curvature of the Sellmeier curve dephases the photon wavepackets.

CONCLUSION

In this work, we have shown that the arrangement of the ligands can significantly affect the effective nonlinearity in MOFs. The difference in the effective nonlinearity was explained based on the hyperpolarizability value calculated for different arrangements of the pyridine ligands in the crystal structure. Our temperature-dependent study revealed that the birefringence value is significantly affected by the alignment of the pyridine rings in the crystal structures; birefringence value increases with decreasing ring alignment (γ°). We also show that there is some correlation between photon pair correlation times and the birefringence as well as ring alignment. Finally, our temperature-dependent methodology can be used to find effective nonlinearity at any given temperature. All these results help in understanding the major contributing factors that can affect entangled photon pair correlation times and provide insight into preparing novel MOFs that are SPDC-efficient.

ASSOCIATED CONTENT

Supporting Information

The Supporting Information is available free of charge at <https://pubs.acs.org/doi/10.1021/acs.jpcc.3c00355>.

NLOSI: Additional tables containing Sellmeier coefficients and dielectric tensors of all the crystal structures; Figures describing all the second-order susceptibility tensors for all the crystal structures and figures describing the birefringence, energy, probability, and Sellmeier curves of different frames extracted from the MD simulations (PDF)

AUTHOR INFORMATION

Corresponding Author

Yamil J. Colón – Department of Chemical and Biomolecular Engineering, University of Notre Dame, Notre Dame, Indiana 46556, United States;  orcid.org/0000-0001-5316-9692; Phone: 1-574-631-8246; Email: ycolon@nd.edu

Authors

Sanoj Raj – Department of Chemical and Biomolecular Engineering, University of Notre Dame, Notre Dame, Indiana 46556, United States;  orcid.org/0000-0002-4876-5921

Rubén A. Fritz – Department of Physics, Universidad de Santiago de Chile, 3493 Santiago, Chile

Felipe Herrera – Department of Physics, Universidad de Santiago de Chile, 3493 Santiago, Chile; ANID Millennium Institute for Research in Optics, 4030000 Concepción, Chile;  orcid.org/0000-0001-8121-1931

Complete contact information is available at:

<https://pubs.acs.org/10.1021/acs.jpcc.3c00355>

Notes

The authors declare no competing financial interest.

ACKNOWLEDGMENTS

Y.J.C. thanks the University of Notre Dame for financial support through start-up funds. F.H. and R.A.F. are supported by ANID through ANID Fondecyt Postdoctoral 3220857, Fondecyt Regular 1221420, and Millennium Science Initiative Program ICN17012. We thank the center for research computing (CRC) at the University of Notre Dame (UND) for computing resources.

REFERENCES

- (1) Karan, S.; Aarav, S.; Bharadhwaj, H.; Taneja, L.; De, A.; Kulkarni, G.; Meher, N.; Jha, A. K. Phase matching in β -barium borate crystals for spontaneous parametric down-conversion. *J. Opt.* **2020**, *22*, 083501.
- (2) Bouwmeester, D.; Pan, J.-W.; Mattle, K.; Eibl, M.; Weinfurter, H.; Zeilinger, A. Experimental quantum teleportation. *Nature* **1997**, *390*, 575–579.
- (3) Pittman, T. B.; Jacobs, B. C.; Franson, J. D. Single photons on pseudodemand from stored parametric down-conversion. *Phys. Rev. A* **2002**, *66*, 042303.
- (4) Wang, J.; Sciarri, F.; Laing, A.; Thompson, M. G. Integrated photonic quantum technologies. *Nat. Photonics* **2020**, *14*, 273–284.
- (5) Walther, P.; Resch, K. J.; Rudolph, T.; Schenck, E.; Weinfurter, H.; Vedral, V.; Aspelmeyer, M.; Zeilinger, A. Experimental one-way quantum computing. *Nature* **2005**, *434*, 169–176.
- (6) Tittel, W.; Brendel, J.; Zbinden, H.; Gisin, N. Quantum Cryptography Using Entangled Photons in Energy-Time Bell States. *Phys. Rev. Lett.* **2000**, *84*, 4737–4740.
- (7) Sergienko, A. V.; Atature, M.; Walton, Z.; Jaeger, G.; Saleh, B. E. A.; Teich, M. C. Quantum cryptography using femtosecond-pulsed parametric down-conversion. *Phys. Rev. A* **1999**, *60*, R2622–R2625.
- (8) Jennewein, T.; Simon, C.; Weihs, G.; Weinfurter, H.; Zeilinger, A. Quantum Cryptography with Entangled Photons. *Phys. Rev. Lett.* **2000**, *84*, 4729–4732.
- (9) Pittman, T. B.; Shih, Y. H.; Strekalov, D. V.; Sergienko, A. V. Optical imaging by means of two-photon quantum entanglement. *Phys. Rev. A* **1995**, *52*, R3429–R3432.
- (10) Strekalov, D. V.; Sergienko, A. V.; Klyshko, D. N.; Shih, Y. H. Observation of Two-Photon “Ghost” Interference and Diffraction. *Phys. Rev. Lett.* **1995**, *74*, 3600–3603.
- (11) D’Angelo, M.; Kim, Y.-H.; Kulik, S. P.; Shih, Y. Identifying Entanglement Using Quantum Ghost Interference and Imaging. *Phys. Rev. Lett.* **2004**, *92*, 233601.
- (12) Boto, A. N.; Kok, P.; Abrams, D. S.; Braunstein, S. L.; Williams, C. P.; Dowling, J. P. Quantum Interferometric Optical Lithography: Exploiting Entanglement to Beat the Diffraction Limit. *Phys. Rev. Lett.* **2000**, *85*, 2733–2736.
- (13) Matthews, J. C.; Zhou, X. Q.; Cable, H.; Shadbolt, P. J.; Saunders, D. J.; Durkin, G. A.; Pryde, G. J.; O’Brien, J. L. Towards practical quantum metrology with photon counting. *npj Quantum Information* **2016**, *2*, 16023.
- (14) Boyd, R. *Nonlinear Opt.*; Elsevier: Burlington, MA, U.S.A., 2008.
- (15) Kurtz, S. K.; Perry, T. T. A Powder Technique for the Evaluation of Nonlinear Optical Materials. *J. Appl. Phys.* **1968**, *39*, 3798–3813.
- (16) Aramburu, I.; Ortega, J.; Folcia, C. L.; Etxebarria, J. Second harmonic generation by micropowders: a revision of the Kurtz-Perry method and its practical application. *Appl. Phys. B: Laser Opt.* **2014**, *116*, 211–233.
- (17) Fiorentino, M.; Spillane, S. M.; Beausoleil, R. G.; Roberts, T. D.; Battle, P.; Munro, M. W. Spontaneous parametric down-conversion in periodically poled KTP waveguides and bulk crystals. *Opt. Express* **2007**, *15*, 7479–7488.
- (18) Shih, Y. Entangled biphoton source - property and preparation. *Rep. Prog. Phys.* **2003**, *66*, 1009–1044.
- (19) Fritz, R. A.; Colón, Y. J.; Herrera, F. Engineering entangled photon pairs with metal–organic frameworks. *Chem. Sci.* **2021**, *12*, 3475–3482.
- (20) Chen, L.-Z.; Huang, Y.; Xiong, R.-G.; Hu, H.-W. Synthesis and structures of two novel non-centrosymmetric metal–organic polymers containing 2-(pyridin-4-yl)-1*H*-imidazole-4,5-dicarboxylic acid ligands. *J. Mol. Struct.* **2010**, *963*, 16–21.
- (21) Ye, Q.; Li, Y.-H.; Song, Y.-M.; Huang, X.-F.; Xiong, R.-G.; Xue, Z. A Second-Order Nonlinear Optical Material Prepared through In Situ Hydrothermal Ligand Synthesis. *Inorg. Chem.* **2005**, *44*, 3618–3625.
- (22) Kwiat, P. G.; Mattle, K.; Weinfurter, H.; Zeilinger, A.; Sergienko, A. V.; Shih, Y. New High-Intensity Source of Polarization-Entangled Photon Pairs. *Phys. Rev. Lett.* **1995**, *75*, 4337–4341.
- (23) Cheng, L. K.; Bosenberg, W. R.; Tang, C. L. Broadly tunable optical parametric oscillation in β -BaB₂O₄. *Appl. Phys. Lett.* **1988**, *53*, 175–177.
- (24) Louisell, W. H.; Yariv, A.; Siegman, A. E. Quantum Fluctuations and Noise in Parametric Processes. I. *Phys. Rev.* **1961**, *124*, 1646–1654.
- (25) Medishetty, R.; Zaręba, J. K.; Mayer, D.; Samoć, M.; Fischer, R. A. Nonlinear optical properties, upconversion and lasing in metal–organic frameworks. *Chem. Soc. Rev.* **2017**, *46*, 4976–5004.
- (26) Mingabudanova, L. R.; Vinogradov, V. V.; Milichko, V. A.; Hey-Hawkins, E.; Vinogradov, A. V. Metal–organic frameworks as competitive materials for non-linear optics. *Chem. Soc. Rev.* **2016**, *45*, 5408–5431.
- (27) Wang, C.; Zhang, T.; Lin, W. Rational Synthesis of Noncentrosymmetric Metal–Organic Frameworks for Second-Order Nonlinear Optics. *Chem. Rev.* **2012**, *112*, 1084–1104.
- (28) Li, Y.; Xu, G.; Zou, W. Q.; Wang, M. S.; Zheng, F. K.; Wu, M. F.; Zeng, H. Y.; Guo, G. C.; Huang, J. S. A Novel Metal–Organic Network with High Thermal Stability Nonlinear Optical and Photoluminescent Properties. *Inorg. Chem.* **2008**, *47*, 7945–7947.
- (29) Evans, O. R.; Lin, W. Crystal Engineering of Nonlinear Optical Materials Based on Interpenetrated Diamondoid Coordination Networks. *Chem. Mater.* **2001**, *13*, 2705–2712.
- (30) Zhang, J. Y.; Wang, Y. Q.; Peng, H. Q.; Cheng, A. L.; Gao, E. Q. Synthesis, structure, and photoluminescence of a zinc(II) coordination polymer with 4-(tetrazol-5-yl)benzoate. *Structural Chemistry* **2008**, *19*, 535–539.
- (31) Chi-Durán, I.; Fritz, R. A.; Urzúa-Leiva, R.; Cárdenas-Jirón, G.; Singh, D. P.; Herrera, F. Anisotropic Band-Edge Absorption of

- Millimeter-Sized Zn(3-ptz)₂ Single-Crystal Metal–Organic Frameworks. *ACS Omega* **2022**, *7*, 24432–24437.
- (32) García-Garfido, J. M.; Enríquez, J.; Chi-Durán, I.; Jara, I.; Vivas, L.; Hernández, F. J.; Herrera, F.; Singh, D. P. Millimeter-Scale Zn(3-ptz)₂ Metal–Organic Framework Single Crystals: Self-Assembly Mechanism and Growth Kinetics. *ACS Omega* **2021**, *6*, 17289–17298.
- (33) Chi-Durán, I.; Enríquez, J.; Manquian, C.; Wrighton-Araneda, K.; Cañon-Mancisidor, W.; Venegas-Yazigi, D.; Herrera, F.; Singh, D. P. pH-Controlled Assembly of 3D and 2D Zinc-Based Metal–Organic Frameworks with Tetrazole Ligands. *ACS Omega* **2018**, *3*, 801–807.
- (34) Momma, K.; Izumi, F. VESTA3 for three-dimensional visualization of crystal, volumetric and morphology data. *J. Appl. Crystallogr.* **2011**, *44*, 1272–1276.
- (35) Stokes, H. T.; Hatch, D. M. FINDSYM: program for identifying the space-group symmetry of a crystal. *J. Appl. Crystallogr.* **2005**, *38*, 237–238.
- (36) Ferrero, M.; Rérat, M.; Kirtman, B.; Dovesi, R. Calculation of first and second static hyperpolarizabilities of one- to three-dimensional periodic compounds. Implementation in the CRYSTAL code. *J. Chem. Phys.* **2008**, *129*, 244110.
- (37) Ferrero, M.; Rérat, M.; Orlando, R.; Dovesi, R. The calculation of static polarizabilities of 1–3D periodic compounds. the implementation in the crystal code. *J. Comput. Chem.* **2008**, *29*, 1450–1459.
- (38) Ferrero, M.; Rérat, M.; Orlando, R.; Dovesi, R. The calculation of static polarizabilities of 1–3D periodic compounds. the implementation in the crystal code. *J. Comput. Chem.* **2008**, *29*, 1450–1459.
- (39) Dovesi, R.; Erba, A.; Orlando, R.; Zicovich-Wilson, C. M.; Civalleri, B.; Maschio, L.; Rerat, M.; Casassa, S.; Baima, J.; Salustro, S.; Kirtman, B. Quantum-mechanical condensed matter simulations with CRYSTAL. *WIREs Comput. Mol. Sci.* **2018**, *8*, e1360.
- (40) Loiko, P.; Becker, P.; Bohatý, L.; Liebald, C.; Peltz, M.; Vernay, S.; Rytz, D.; Serres, J. M.; Mateos, X.; Wang, Y.; et al. Sellmeier equations, group velocity dispersion, and thermo-optic dispersion formulas for CaLnAlO₄ (Ln = Y, Gd) laser host crystals. *Opt. Lett.* **2017**, *42*, 2275–2278.
- (41) Thompson, A. P.; Aktulga, H. M.; Berger, R.; Bolintineanu, D. S.; Brown, W. M.; Crozier, P. S.; in 't Veld, P. J.; Kohlmeyer, A.; Moore, S. G.; Nguyen, T. D.; et al. LAMMPS - a flexible simulation tool for particle-based materials modeling at the atomic, meso, and continuum scales. *Comput. Phys. Commun.* **2022**, *271*, 108171.
- (42) Boyd, P. G.; Moosavi, S. M.; Witman, M.; Smit, B. Force-Field Prediction of Materials Properties in Metal-Organic Frameworks. *J. Phys. Chem. Lett.* **2017**, *8*, 357–363.
- (43) Frisch, M. J.; Trucks, G. W.; Schlegel, H. B.; Scuseria, G. E.; Robb, M. A.; Cheeseman, J. R.; Scalmani, G.; Barone, V.; Petersson, G. A.; Nakatsuji, H. P.; et al. *Gaussian 16*, Revision C.01.; Gaussian Inc.: Wallingford, CT, 2016.
- (44) Stobier, R. E.; Moore, S. A. *Biaxial Crystal Optics*; Springer US: Boston, MA, 1994; pp 159–171.
- (45) Lu, J.; Lian, Y. K.; Xiong, L.; Wu, Q. R.; Zhao, M.; Shi, K. X.; Chen, L.; Wu, L. M. How To Maximize Birefringence and Nonlinearity of π -Conjugated Cyanurates. *J. Am. Chem. Soc.* **2019**, *141*, 16151–16159.
- (46) Lee, D.; Kim, I.; Lee, K. J. Investigation of 1064-nm Pumped Type II SPDC in Potassium Niobate for Generation of High Spectral Purity Photon Pairs. *Crystals* **2021**, *11*, 599.
- (47) Barnes, N. P.; Gettemy, D. J.; Adhav, R. S. Variation of the refractive index with temperature and the tuning rate for KDP isomorphs. *J. Opt. Soc. Am.* **1982**, *72*, 895–898.
- (48) Schlarb, U.; Betzler, K. Refractive indices of lithium niobate as a function of temperature, wavelength, and composition: A generalized fit. *Phys. Rev. B* **1993**, *48*, 15613–15620.
- (49) Nikogosyan, D. N. Beta barium borate (BBO). *Appl. Phys. A: Mater. Sci. Process.* **1991**, *52*, 359–368.
- (50) Cheng, M.; Wu, S.; Zhu, Z. Z.; Guo, G. Y. Large second-harmonic generation and linear electro-optic effect in trigonal selenium and tellurium. *Phys. Rev. B* **2019**, *100*, 035202.

■ NOTE ADDED AFTER ASAP PUBLICATION

This paper published ASAP on May 30, 2023 with a production error in eq 1. The error was corrected and the revised paper reposted on June 1, 2023.